

Enhancing Speckle Statistics for Imaging Inside Scattering Media

WEI-YU CHEN¹, MATTHEW O'TOOLE¹, ASWIN C. SANKARANARAYANAN¹, AND ANAT LEVIN^{2,*}

¹Carnegie Mellon University, 5000 Forbes Avenue Pittsburgh, PA 15213

²Technion, Israel, Technion City, Haifa 3200003, Israel

*Corresponding author: anat.levin@ee.technion.ac.il

Compiled July 19, 2022

We exploit memory effect correlations in speckles for the imaging of incoherent fluorescent sources behind scattering tissue. These correlations are often weak when imaging thick scattering tissues and complex illumination patterns, both of which greatly limit the practicality of associated techniques. In this work, we introduce a spatial light modulator between the tissue sample and the imaging sensor and capture multiple modulations of the speckle pattern. We show that, by correctly designing the modulation patterns and the associated reconstruction algorithm, the statistical correlations in the measurements can be greatly enhanced. We exploit this to demonstrate the reconstruction of mega-pixel sized fluorescent patterns behind the scattering tissue. © 2022 Optica Publishing Group

<http://dx.doi.org/10.1364/ao.XX.XXXXXX>

1. INTRODUCTION

Scattering of light is one of the main barriers preventing the imaging of fluorescent sources located deep inside biological tissue. A microscope imaging a set of incoherent sources inside the tissue usually observes a noisy speckle pattern that has little resemblance to the actual sources.

Despite the noise-like appearance, speckle has strong statistical properties, such as the *memory effect* (ME), implying that the patterns generated by nearby sources are correlated. It has been previously observed that due to this ME correlation, the auto-correlation of a speckle pattern generated by multiple independent sources is equivalent to the auto-correlation of the latent source layout [1–10]. This fascinating property has drawn a lot of interest since it allows the recovery of latent illuminators, completely invisible to the naked eye, purely by exploiting speckle statistics.

Despite its potential, there are still major challenges to solve before the idea can apply to realistic biomedical imaging scenarios. The main barrier is that ME correlations are very weak and the amount of information that can be inferred from them is limited. To circumvent this, past experimental demonstrations have made use of various simplifying assumptions. While fluorescent sources of interest in realistic biomedical imaging scenarios are located inside the scattering sample rather than far behind it, most demonstrations of speckle correlation-based see-through algorithms consider sources located a few centimeters beyond the sample. This is due to the fact that when the sources are further from the scattering layer [11], they span a smaller range of angles relative to the sample and therefore speckle correla-

tions are stronger. A second issue is that the contrast of the observed speckle pattern decays as more independent emitters are present, and hence, the technique is mostly applicable to very sparse emitter layouts.

In this work, we exploit strategies for maximizing the amount of ME correlation we can extract from speckle images. To this end, we build on a simple observation: imaging the same layout of fluorescent sources through different tissue layers would allow us to obtain independent speckle images, thereby leading to independent auto-correlations. Averaging such independent auto-correlations can suppress noise in the correlations and boost the quality of the illuminator patterns that we can infer from it. While some temporal dynamics are present in live tissue, sequential images of illuminators inside the same tissue are still highly correlated. Rather, we use a programmable spatial light modulator (SLM) mask in the optical path imaging the tissue and use it to modulate the field, leading to different speckle images. We discuss various forms of modulation and arrive at a spatial form of modulation we term *translating interferometry*. We show that despite the fact that we image the same tissue layer multiple times, we can get uncorrelated measurements that maximize ME correlation.

To further maximize the amount of information that we can extract from speckle data, we follow an idea recently proposed by [11], which argues that when light sources are located inside the sample rather than far behind it, the speckle pattern generated by each source has a limited support and does not spread over the full sensor. Thus, rather than computing a global full-frame auto-correlation, they compute local auto-correlations in the form of a Ptychography algorithm [12–16]. These local

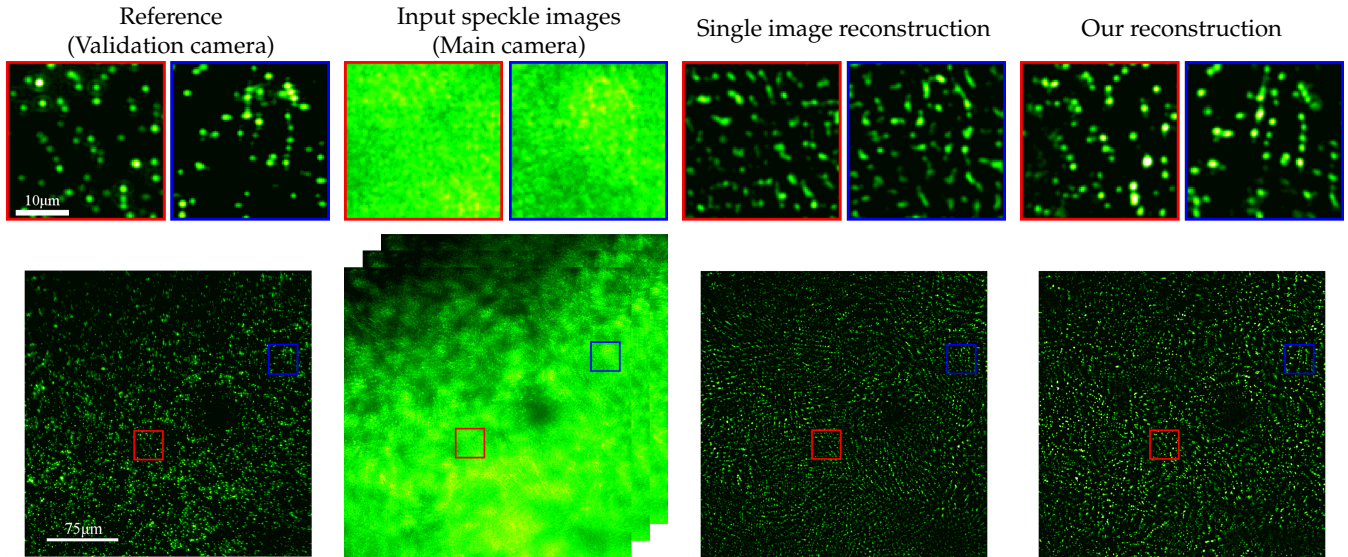


Fig. 1. Reconstructing a wide-range fluorescent bead target from modulated speckles. We reconstruct the layout of fluorescent beads spread behind a chicken breast tissue slice, whose thickness was measured at about $\sim 150\mu\text{m}$. The beads are attached to the tissue, separated only by a $150\mu\text{m}$ cover glass. The beads spread over a field of view of $300\mu\text{m} \times 300\mu\text{m}$, occupying a one mega pixel image. While the ME correlations in a single image capture are too noisy to provide good reconstruction, we optically modulate the speckle field, capturing 54 shots with different modulations. This modulation allows us to amplify statistical correlations, leading to accurate reconstruction of a complex illuminator pattern, despite high degradation and limited speckle contrast in the input images. The lower part of the figure includes the full images, while at the top we zoom on two sub windows for high resolution visualization.

correlations can boost the signal to noise ratio of the detected correlation by a few orders of magnitude.

Overall, we demonstrate the reconstruction of wide, complex fluorescent bead patterns inside scattering tissue. Our approach captures only a few dozen images of the tissue, compared to hundreds of images used by recent approaches that image fluorescent sources behind scattering layers [17, 18] when using single-photon fluorescent emission; which is linear with respect to excitation energy. Compared to recent wavefront shaping approaches [19, 20] that only facilitate imaging of a local neighborhood governed by the limited extent of the ME, our approach recovers mega-pixel images over a wide field of view, as demonstrated in Fig. 1.

2. PRINCIPLE

A. A review of ME-based imaging

We start with a quick review of the ME and its application for seeing inside scattering media. Let $\mathbf{i}^1, \mathbf{i}^2$ denote the position of two illumination sources and $u^{\mathbf{i}^1}(\mathbf{v}), u^{\mathbf{i}^2}(\mathbf{v})$ the fields they generate, where \mathbf{v} denotes a sensor coordinate. The ME states that speckle fields generated by *nearby* sources are related by a tilt-shift correlation [21]. Recently, Bar *et al.* [22] have offered a simple model for this relation, stating that

$$u^{\mathbf{i}^1}(\mathbf{v}) \approx e^{ik\alpha\langle\Delta, \tau\rangle} u^{\mathbf{i}^2}(\mathbf{v} + \Delta), \quad (1)$$

with $\Delta = \mathbf{i}^2 - \mathbf{i}^1$ the displacement between the sources, $\tau = \mathbf{v} - \mathbf{i}^1$ the displacement between the source to the observation point, and $\alpha \approx \frac{-3}{2L}$, where L is the tissue thickness. This model assumes that we image the volume with a microscope whose sensor plane is conjugate to the plane of the illuminators $\mathbf{i}^1, \mathbf{i}^2$.

An image sensor only measures the intensity of the speckle pattern which we denote by

$$S^{\mathbf{i}^n}(\mathbf{v}) = |u^{\mathbf{i}^n}(\mathbf{v})|^2. \quad (2)$$

In the presence of multiple incoherent illuminators, we observe an intensity image $I(\mathbf{v}) = \sum_n S^{\mathbf{i}^n}(\mathbf{v}) = \sum_n |u^{\mathbf{i}^n}(\mathbf{v})|^2$. Assuming source displacements are small enough for ME correlation to hold, speckle intensities from nearby sources are shifted versions of each other, $S^{\mathbf{i}^1}(\mathbf{v}) \approx S^{\mathbf{i}^2}(\mathbf{v} + \Delta)$. Note that since we deal with intensity images, phase adjustments are not required.

We denote by $S^0(\mathbf{v})$ the speckle from an illumination source at the center of the frame. With this notation, we can express the sum of speckles from incoherent sources as

$$I = S^0(\mathbf{v}) * O, \quad (3)$$

where O is a binary image denoting the location of the illumination sources, and $*$ denotes convolution. To detect fluorescent sources through scattering media, our goal is to recover the latent illuminator pattern O from an input speckle image I .

We now filter I and S^0 to locally have a zero mean

$$\bar{I} = I - g * I, \quad \bar{S}^0 = S^0 - g * S^0, \quad (4)$$

where g is a low pass filter. We note that Eq. (3) also holds if we replace I, S^0 with \bar{I}, \bar{S}^0 , and we can express $\bar{I} = \bar{S}^0 * O$. Since \bar{S}^0 is a random zero mean signal, its auto-correlation is approximately an impulse function [2]

$$\bar{S}^0 * \bar{S}^0 \approx \delta. \quad (5)$$

With this approximation [1, 2] derive the relationship:

$$\bar{I} * \bar{I} = (\bar{S}^0 * \bar{S}^0) * (O * O) \approx O * O, \quad (6)$$

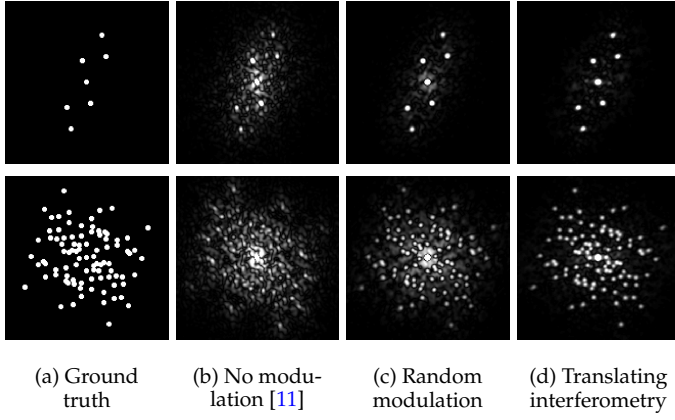


Fig. 2. Comparing speckle auto-correlation with different modulation approaches. The two rows compare illuminator layouts with different complexities, while the columns evaluate different modulation strategies. All results use the same number of shot images. (a) Ground truth auto-correlation. (b) Without any modulation, reconstructed auto-correlation is noisy, and when the target is complex (2nd row), it is almost unrecognizable. (c) Random modulation can improve contrast, but still contains noise. (d) Translating interferometry can clearly recover the auto-correlation.

where \star denotes cross correlation. Thus, the auto-correlation of the input speckle intensity is equivalent to the auto-correlation of the desired latent image O . As a result, one can recover O from $\bar{I} \star \bar{I}$ using a phase retrieval algorithm [2].

Challenges. The observation made by Eq. (6) is very compelling because it suggests that latent illuminators O can be recovered from a noisy speckle image I , despite the fact that to the untrained eye, the input images carry no similarity to the latent source layout. Yet, it involves two major assumptions that limit its practical applicability.

The first problem is that the ME correlation is not exact, especially when the displacement between the illuminators increase. A second problem is that since the speckle pattern S^0 emerging from a single source has a limited support and only spans a finite number of pixels, its auto-correlation outlined in Eq. (5) is not a perfect impulse, but involves residual noise. Effectively, in realistic scenarios, $\bar{I} \star \bar{I}$ is a *very* noisy approximation to $O \star O$. This noise increases as more independent illuminators are present in O .

In Fig. 2(b), we show the auto-correlation of a speckle image \bar{I} composed of a sparse layout of sources. We compare two layouts with a different number of sources. We can see that as more incoherent sources are included, the auto-correlation is very noisy and does not resemble $O \star O$. Our goal in this work is to improve the contrast of this auto-correlation by capturing multiple modulations of the speckle signal.

B. Improving auto-correlation contrast

To analyze the contrast of the speckle correlation, we introduce the following notation. We denote by Γ_Δ the set of all displacements Δ , such that our latent pattern includes a pair of illuminators (n, m) displaced by Δ :

$$\Gamma_\Delta = \{\Delta | \exists (n, m), \Delta = \mathbf{i}^m - \mathbf{i}^n\}, \quad (7)$$

and by Γ_Δ^c the list of all other displacements. We denote the speckle auto-correlation by $\mathcal{C}^{\bar{I}}$, which is defined for a displace-

ment Δ as:

$$\mathcal{C}^{\bar{I}}(\Delta) = \sum_{\mathbf{v}} \bar{I}(\mathbf{v}) \bar{I}(\mathbf{v} + \Delta). \quad (8)$$

Intuitively, the speckle correlation has good contrast if $\mathcal{C}^{\bar{I}}(\Delta)$ is high for displacements $\Delta \in \Gamma_\Delta$, corresponding to real illuminator positions; and is low for all other displacements $\Delta \in \Gamma_\Delta^c$. We define the correlation contrast using the following signal to noise metric:

$$\Theta(\mathcal{C}^{\bar{I}}) = \frac{\frac{1}{|\Gamma_\Delta|} \sum_{\Delta \in \Gamma_\Delta} \mathbb{E}[\mathcal{C}^{\bar{I}}(\Delta)]^2}{\frac{1}{|\Gamma_\Delta^c|} \sum_{\Delta \in \Gamma_\Delta^c} \text{Var}[\mathcal{C}^{\bar{I}}(\Delta)]} \quad (9)$$

One way to increase the correlation contrast used by [1], is to capture multiple images of the latent pattern O behind different scattering layers. Effectively, we measure $I_t = S_t^0 \star O$ with different speckle patterns S_t^0 . The auto-correlation is then evaluated as the average of the individual auto-correlations

$$\mathcal{C}^{\bar{I}_1, \dots, \bar{I}_T}(\Delta) = \frac{1}{T} \sum_t \mathcal{C}^{\bar{I}_t}(\Delta), \quad (10)$$

with $\mathcal{C}^{\bar{I}_t} = \bar{I}_t \star \bar{I}_t$ as defined in Eq. (8).

In supplement Sec. A.A, we formally prove the following.

Claim 1 *If the speckle patterns S_t^0 are uncorrelated with each other for different t values, then replacing $\mathcal{C}^{\bar{I}}$ with $\mathcal{C}^{\bar{I}_1, \dots, \bar{I}_T}$ in the correlation contrast of Eq. (9) increases the contrast linearly with the number of measurements T , i.e.,*

$$\Theta(\mathcal{C}^{\bar{I}_1, \dots, \bar{I}_T}) = T \cdot \Theta(\mathcal{C}^{\bar{I}}). \quad (11)$$

While this is a promising idea, when the sources are located inside the tissue, it is not easy to image the same illuminators through different scattering layers. Rather, in this work, we would like to modify the speckle pattern by adjusting the optics.

Random modulation. Intuitively, to create different speckle intensity images, we can put a random phase mask in the optical path between the sample to the imaging sensor. If we put this mask in the Fourier plane, it would translate into a convolution of the fields $u^i(\mathbf{v})$ with the Fourier transform of the mask, which we denote as h_t . This would lead into an intensity image $I_t = \sum_n S_t^n$ with

$$S_t^n = |u^{i^n} \star h_t|^2. \quad (12)$$

In Fig. 2(c), we compare the auto-correlation of a single speckle image to the average auto-correlation with 54 random masks h_t . Averaging random masks rejects noise and improves the correlation contrast, but it is still noisy.

To understand why random modulation is sub-optimal, we review the tilt-shift correlation in Eq. (1). If the fields u^{i^1}, u^{i^2} generated by different illuminators would follow a pure shift, then $u^{i^1} \star h_t, u^{i^2} \star h_t$ would also be shifted versions of each other. However, according to Eq. (1), fields from different sources vary by phase, and hence a convolution with h_t largely degrades the correlation and $S_t^{i^1}(\mathbf{v})$ would differ from $S_t^{i^2}(\mathbf{v} + \Delta)$.

Translating interferometry. Our goal in this work is to change the optical path such that we can capture multiple uncorrelated speckle patterns, and yet maintain the ME correlation. To this end, we design an interferometric setup that allows us to measure the interference between u^{i^n} and a shifted copy of it, which

we name *translating interferometry*. This leads to a measurement of the form

$$S_t^{i^n} = u^{i^n}(\mathbf{v})u^{i^n}(\mathbf{v} + \mathbf{d}_t)^*, \quad (13)$$

where \mathbf{d}_t denotes the displacement vector. We acquire these measurements using an incoherent interferometry scheme, described in supplement Sec. A.C.

When several incoherent sources are present, we will acquire an incoherent summation

$$I_t = \sum_n S_t^{i^n}. \quad (14)$$

This interferometric measurement is already a zero mean signal and there is no need to subtract the mean as with the intensity measurements of Eq. (4).

The translating interferometry measurements provide two main benefits which we summarize in the following claims and prove in supplement Sec. A.A. First, unlike a naive optical mask in Eq. (12), it does not reduce the ME correlation of the original speckles. Second, despite the fact that these measurements are captured from the same tissue layer and they are not independent, they are still *uncorrelated*.

Claim 2 For displacements in the order of a few speckle grains, the correlation between translating interferometry signals $S_t^{i^1}, S_t^{i^2}$ produced by different illuminators $\mathbf{i}^1, \mathbf{i}^2$ is approximately the same as the correlation of the original speckle intensity images.

Claim 3 For displacements $\mathbf{d}_{t_1}, \mathbf{d}_{t_2}$ whose distance $\|\mathbf{d}_{t_1} - \mathbf{d}_{t_2}\|$ is larger than the speckle grain, the signals $S_{t_1}^{i^n}, S_{t_2}^{i^n}$ are uncorrelated.

The observation in Claim 3 is central for this paper. The fact that different displacements lead to uncorrelated speckle measurements means that according to Claim 1, we could average them and the auto-correlation contrast would improve *linearly* with the number of measurements.

The auto-correlation of the translating interferometry measurements relates to the auto-correlation of the hidden illuminator pattern O , but unlike pure intensity speckles, with the above modulations a phase correction is needed, which we derive in the following claim, and prove in supplement Sec. A.A.

Claim 4 Using the translating interferometry measurements of Eq. (13), the speckle auto-correlation $\mathcal{C}^{I_t} = I_t \star I_t$ approximates the auto-correlation of the latent pattern $\mathcal{C}^O = O \star O$, times a phase ramp correction

$$\mathcal{C}^{I_t}(\Delta) \approx e^{-jk\alpha \langle \Delta, \mathbf{d}_t \rangle} \mathcal{C}^O(\Delta). \quad (15)$$

Given the relation in Claim 4, we average the auto-correlation of the different translating interferometry measurements, applying the phase ramp correction of Eq. (15):

$$\mathcal{C}^{I_1, \dots, I_T} = \frac{1}{T} \sum_t e^{jk\alpha \langle \Delta, \mathbf{d}_t \rangle} \mathcal{C}^{I_t}(\Delta) \quad (16)$$

The phase corrected averaging in Eq. (16) is subject to a single unknown parameter α . In our implementation, we manually tune it to maximize the visual quality of the results.

Analyzing translating interferometry correlations. In Fig. 2(d) we show the auto-correlation obtained by averaging translating interferometry measurements I_t (Eq. (14)) with the phase ramp correction of Eq. (16). Our approach reduces noise and improves the correlation contrast when compared with random modulations (Eq. (12)) or just with the auto-correlation of a single speckle image.

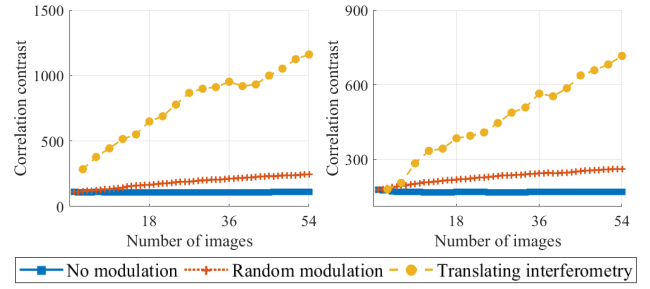


Fig. 3. Contrast improvement for different modulations. We compare speckle correlation contrast as a function of the number of images for different modulation approaches. The two images show correlation contrast measurements for two different tissue slices. The graphs are noisy due to the finite speckle spread in an image, but still demonstrate clear differences between different modulation approaches. Without modulation, multiple images only reduce read and photon noise of the image, which does not lead to a significant improvement in contrast. Multiple images with random modulations can improve contrast, but the gain saturates quickly as ME degrades. On the other hand, translating interferometry can achieve a higher contrast, and, in agreement with theory, contrast increases roughly linearly with the number of shots.

Table 1. Summary of different speckle modulation approaches.

	$S_t^{i^n}$	Averaged auto-correlation
No modulation [11]	$ u^{i^n}(\mathbf{v}) ^2$	$\mathcal{C}^{I_t}(\Delta)$
Random modulation	$ u^{i^n}(\mathbf{v}) * h_t ^2$	$\frac{1}{T} \sum_t \mathcal{C}^{I_t}(\Delta)$
Translating interf.	$u^{i^n}(\mathbf{v})u^{i^n}(\mathbf{v} + \mathbf{d}_t)^*$	$\frac{1}{T} \sum_t e^{jk\alpha \langle \Delta, \mathbf{d}_t \rangle} \mathcal{C}^{I_t}(\Delta)$

In Fig. 2(d), we average 18 translating interferometry measurements I_t . Note that as we explain in supplement Sec. A.C, capturing each interferometric measurement I_t requires 3 shots, so the 18 measurements in Fig. 2(d-e) are acquired using a total of 54 shots. This is compared against 54 independent measurements captured by the random modulation approach. The 18 translating interferometry modulations are superior over the 54 random modulations.

We note that the translating interferometry measurements used here are similar to those used in shearing interferometry [23]. However, shearing interferometry usually uses smaller displacements to obtain the local gradient of the wave, while the displacements we use here are larger than the speckle grain size so that we obtain uncorrelated speckles.

Table 1 summarizes the different modulation approaches evaluated in this paper. In Fig. 3 we plot the correlation contrast of Eq. (9) as a function of the number of averaged images T . We start by capturing multiple images without any modulation. This only reduces read and photon noise, which does not translate into a real improvement in correlation contrast. When we randomly modulate the wave (Eq. (12)), the contrast increases but it eventually saturates as the convolution reduces the ME correlation. By using our translating interferometry (Eq. (13)), the contrast increases roughly linearly as predicted by the theory. This suggests that the speckle signals S_t we generate are indeed uncorrelated for different displacements $\mathbf{d}_{t_1}, \mathbf{d}_{t_2}$. The graphs in

Fig. 3 demonstrate correlation contrast observed with two different tissue slices. For each of the tissue slices, we generated the source layout in the top row of Fig. 2. As we evaluate speckles through real tissue, we note that: 1) the exact amount of correlation we measure in each tissue slice can vary, and 2) each tissue layer generates a speckle spread with a limited support. As we only average a finite number of speckle pixels, the graphs are noisy. Despite these issues, the graphs measured from difference slices demonstrate consistent trends.

C. Exploiting local support

The previous section aims to increase the auto-correlation contrast by averaging multiple measurements. To improve on it, we adopt a complementary approach for noise reduction, recently suggested by [11]. This approach is based on the observation that when the light sources are inside the sample, rather than far behind it, the speckle pattern scattered from a single source has *local support*, *i.e.*, the scattered light does not spread over the entire sensor. Therefore, it is argued that computing the full-frame auto-correlation over the entire image corrupts the signal with additional noise. Rather, it is sufficient to match between the local correlations of the observed speckle pattern and the optimized latent image. This leads into a Ptychography style cost [24]. We review the exact cost in supplement Sec. A.B. In the experimental section below, we show that moving from full-frame correlations to local ones has a major impact on noise elimination and improving the resulting reconstruction.

Another advantage of the local cost discussed in [11], is that it allows recovering patterns larger than the extent of the ME. As mentioned above, ME correlations of the form of Eq. (1) only hold for small displacements Δ . When matching the full-frame auto-correlation (Eq. (6)) of I and O , we rely on the fact that ME correlation exists between any two sources in our latent pattern. This assumption largely limits the range of recoverable illuminator patterns to patterns lying within the ME range. In contrast, the local cost only relies on local correlations between sources in the same local window. At the same time, the overall extent of the illuminator pattern O can be larger than these local windows.

3. RESULTS

A. Experiment setup

Fig. 4 illustrates our acquisition setup, including an imaging arm and a validation arm. The imaging arm consists of an objective and a tube lens, followed by a second relay system which allows us to place a spatial light modulator (SLM) at the Fourier plane. The image of the modulated field is collected by the main camera. The objective attempts to image incoherent sources beyond a scattering sample. A second validation camera images the beads from the other end of the tissue, allowing the capture of a clear unscattered image of the illuminator layout, which is used to assess reconstruction quality. Note that this validation camera does not provide any input to the algorithm. The target and the validation objectives are mounted on z-axis translation stages, facilitating accurate control over focusing in both imaging and validation arms.

For most of our experiments, we used chicken breast tissue as a scattering sample. In the supplement, we also demonstrate results imaging through a parafilm tissue phantom. We discuss what is known about the optical characterization of these materials in supplement Sec. A.H. We used Spherotech Fluorescent Nile Red Particles 0.4 – 0.6 μm , FP-0556-2. The beads

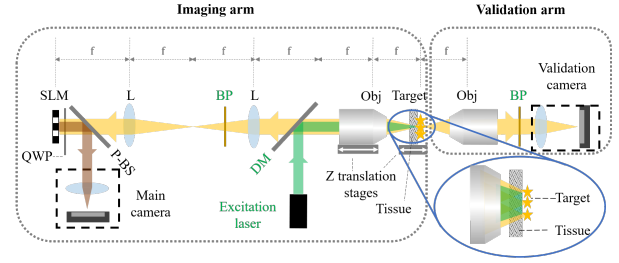


Fig. 4. Experimental setup. L: lens. Obj: objective lens. BP: bandpass filter. QWP: quarter wave plate. P-B: polarized beam splitter. DM: dichromatic mirror. We attach fluorescent beads at the back of a tissue layer. A laser excites the beads from the front side of the tissue. The emitted light is back scattered through the tissue and collected by the main camera. We create a 4f relay system in the optical path and place an SLM in its Fourier plane to modulate the scattered light. Finally, we used a validation camera behind the tissue which can image the beads directly. This camera is not part of our algorithm and is only used to validate its output.

are attached on a microscope cover glass behind the scattering tissue. The separation between the beads and the tissue is as low as 150 μm , the thickness of the cover glass. The beads are excited with a 530nm laser from the front side of the tissue. The excitation light scatters through the tissue, illuminates the beads, and the emitted light scatters back through the tissue to the camera. We filtered the excited light using a 10nm bandpass filter centered at 580nm.

Throughout the experimental section, we visualize the fluorescent bead captures with a green colormap. We use a red colormap to visualize images from an alternative setup described in supplement Sec. A.D. Such images are captured through real tissue but the source layout is computer-synthesized.

B. Experiment results

We start by demonstrating our setup on a fluorescent bead target. In Fig. 1, we reconstruct a 1000 \times 1000 pixel image, corresponding to a field of view of 300 μm \times 300 μm . The random beads were spread behind a \sim 150 μm thick tissue. Note that all thickness measurements in this paper are approximated due to the limited resolution of the clipper. The bead layout is unrecognizable from the captured speckle input. Moreover, as so many independent incoherent sources are present, the input images are rather smooth and speckle variation is almost invisible. Despite this, our translating interferometry framework achieves a clear reconstruction from 54 shots. Fig. 5 demonstrates another reconstruction of beads behind a \sim 150 μm thick tissue. Fig. 6 demonstrates a reconstruction of structured patterns rather than sparse beads. Details about this target are provided in supplement Sec. A.D.

While the reference and the reconstruction have the same layout they have somewhat different brightness and resolution. The resolution of the reference is subject to the diffraction limit. The reconstruction algorithm on the other hand encourages sparse results, and hence, recovered dots tend to be narrower. The brightness variation is partially attributed to the fact that the reference is captured by a different camera from a different direction, but also due to imperfect convergence of our optimization.

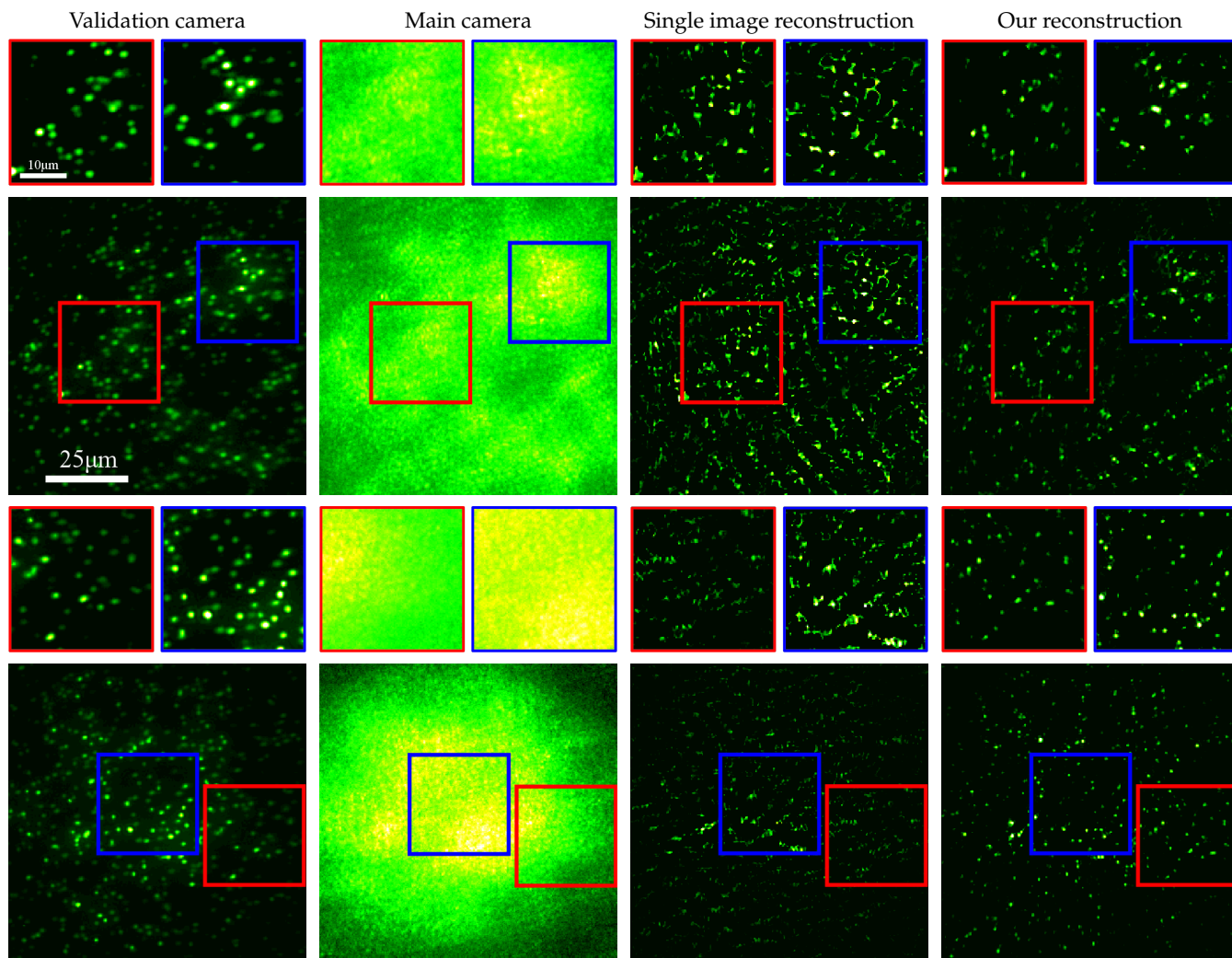


Fig. 5. Reconstruction results for fluorescent beads behind $\sim 150\mu\text{m}$ -thick tissue slices. With translating interferometry, we can clearly reconstruct fluorescent bead targets from 54 shot images captured by the main camera. The reconstruction is compared against a reference image from the validation camera observing the beads directly. In contrast, a standard single-image shot of the scattered light only facilitates a very noisy reconstruction.

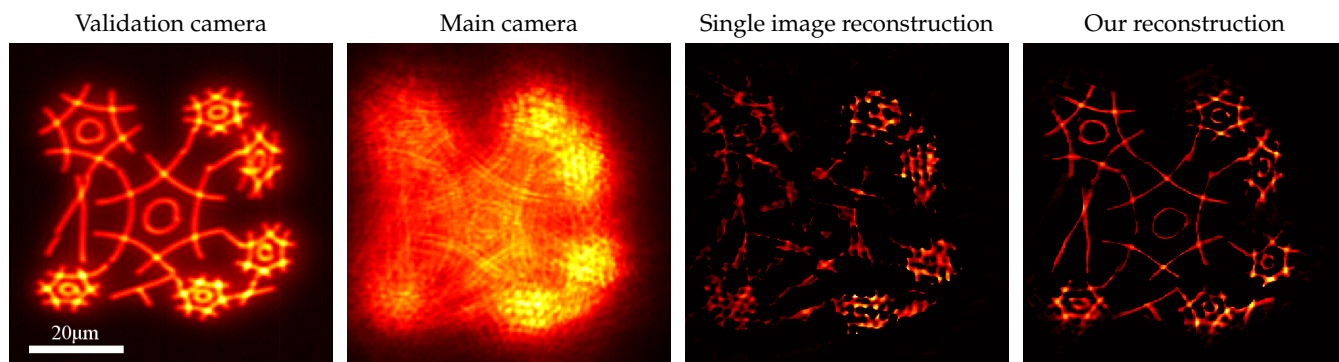


Fig. 6. Reconstruction results from a spatially incoherent target. We reconstruct a spatially incoherent target with a more complicated layout behind $\sim 150\mu\text{m}$ -thick tissue slice.

C. Comparing reconstruction and modulation approaches

In Fig. 7, we evaluate two components of our algorithm: (i) the usage of local correlations [11] discussed in Sec. 2.C, versus the

standard full frame auto-correlation used in previous work [1, 2, 10], and (ii) the modulation approach.

As discussed in [11] and reviewed in Sec. 2.C, the local ap-

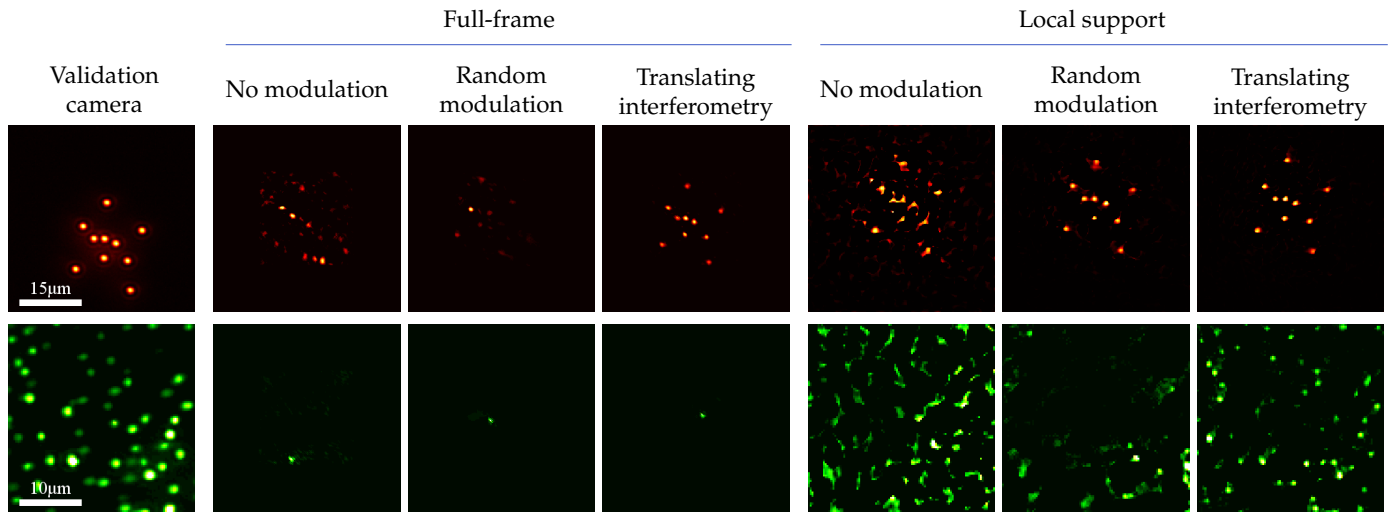


Fig. 7. Comparing reconstruction and modulation approaches. Top part: a spatially incoherent target with a sparse and simple layout. Lower part: challenging fluorescent beads target. Local support correlations [11] are stronger than standard full-frame auto-correlations [10], and our translating interferometry improves over a single shot (with no modulation) and over simple random modulation. For the simple target on the top, the full-frame algorithm can recover the image given the improved correlation provided by translating interferometry modulations, but fails to do so from the noisier correlations provided by other modulation strategies. The local correlation approach which is more robust to noise can recover the target even with the simpler modulations. For the challenging target at the lower part, the full-frame algorithm fails completely using all types of modulations. The local correlations algorithm can reconstruct the target using translating interferometry modulations. However given random modulations, it can only reconstruct a subset of the beads.

proach detects correlations with a higher SNR compared to the full frame approach and indeed it leads to better reconstructions. We also show that the translating interferometry modulation leads to better results compared to simpler modulation alternatives.

Fig. 7 compares different modulation schemes, as well as evaluates the effectiveness of full-frame and local-correlation algorithms. The top row of the figure shows reconstructions of a spatially-incoherent target with a simple structure. For the full frame approach, a single shot results in unrecognizable reconstruction, that is only slightly improved given 54 random modulations. In contrast, our translating interferometry can correctly reconstruct the pattern. The usage of local correlations compared to full-frame ones reduces some of the noise, and hence even random modulations can lead to good reconstruction.

The bottom row of the figure compares reconstructions on a denser fluorescent bead target. As explained in [11], the increased source density is more challenging to reconstruct as the contrast of the incoherent speckle image decreases. The full-frame approach fails to reconstruct this target with any of the modulation approaches. The local correlation algorithm fails with a single shot (no modulation). The random modulation reconstructed only a subset of the beads, and the best results are obtained using translating interferometry modulations.

D. Evaluating reconstruction vs. number of images

Fig. 3 numerically evaluates the correlation contrast improvement as a function of the number of images. In Fig. 8, we visually compare reconstructions using an increasing number of input images, and demonstrate how the improved contrast translates into better reconstruction quality. This experiment uses the same bead layout as in the lower part of Fig. 7, please refer to

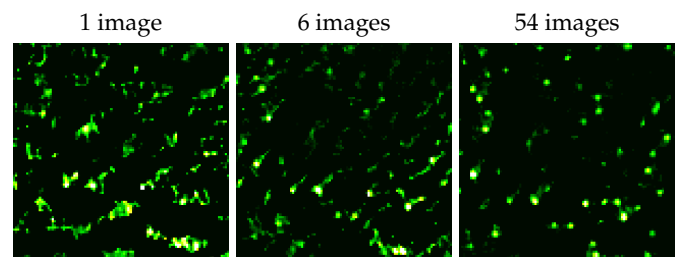


Fig. 8. Evaluating reconstruction vs. number of shots. We visualize the quality of the reconstruction given no modulation (single shot), and with an increasing number of modulation patterns. As evaluated numerically in Fig. 3 the correlation contrast increases linearly with the number of shots and in agreement, the visual quality of the reconstruction improves. The reference speckle layout in this experiment is equivalent to the validation camera image in the lower part of Fig. 7.

the validation camera reference displayed there.

4. DISCUSSION

In this work, we demonstrate the reconstruction of fluorescent illuminator patterns attached to a scattering tissue. Despite heavy scattering that completely distort the captured images, we can exploit ME correlations in the measured speckles to detect the hidden illuminator layout. While such correlations are inherently weak, we suggest a modulation scheme which allows us to capture multiple uncorrelated speckle measurements of the same sources. By averaging the correlations of such measurements, we increase the signal to noise ratio in the data and largely boost the reconstruction quality. We combine these modulated

measurements with a recent algorithm [11] seeking a latent pattern whose local correlations agree with local correlations in the measured data. The local correlations provide additional improvement in SNR. Moreover, since it only assumes local correlations between the speckles emitted by nearby sources rather than global full-frame correlations between any two sources in the image, it allows us to reconstruct wide patterns, much beyond the limited extent of the ME. Overall, we demonstrate the reconstruction of mega-pixel wide patterns, limited only by the sensor size.

Despite the advances offered by this approach, it is inherently dependent on the existence of some ME correlation; thus when such correlations are too weak to be measured, our approach will fail as well. Two major factors that decrease the ME correlations are the tissue thickness and the number of independent incoherent sources. In our current implementation, we recovered sources behind $150\mu\text{m}$ -thick tissue, which is beyond the penetration depth of a standard microscope. While this significantly advances the capabilities of a standard microscope, numerous biomedical applications would benefit from increasing this depth further. The second challenge for ME-based correlations is that we assume speckle variation is observed in the captured data. As more and more independent sources are present, the speckle contrast decays and the captured intensity images are smoother. Naturally, when speckle contrast is lower than the photon noise in the data, no correlations can be detected. Hence ME-based techniques are inherently limited to simple, sparse illuminator layouts.

An alternative approach for seeing through scattering tissue is based on wavefront shaping optics. Rather than post-process the speckle data, it attempts to modulate the incoming excitation light and/or the outgoing emission, to undo the tissue aberration in optics. In theory, this approach carries the potential to extend to thicker tissue layers and to correct complex patterns. In practice, efficiently finding a proper modulation mask is a challenging task. Recently, [20] has managed to recover such a modulation efficiently using linear (single photon) fluorescent feedback from a sparse set of beads. However, even after recovering a good modulation mask, the area they could correct with it is limited due to the limited extent of the ME. In contrast, our approach can recover wide-field-of-view, full-frame images, as it only relies on local ME correlations.

Disclosures. The authors declare no conflicts of interest.

Supplemental document. See Supplement 1 for supporting content.

REFERENCES

- O. Katz, P. Heidmann, M. Fink, and S. Gigan, "Non-invasive single-shot imaging through scattering layers and around corners via speckle correlation," *Nat. Photonics* (2014).
- J. Bertolotti, E. G. van Putten, C. Blum, A. Lagendijk, W. L. Vos, and A. P. Mosk, "Non-invasive imaging through opaque scattering layers," (2012).
- K. T. Takasaki and J. W. Fleischer, "Phase-space measurement for depth-resolved memory-effect imaging," *Opt. Express* (2014).
- E. Edrei and G. Scarcelli, "Optical imaging through dynamic turbid media using the fourier-domain shower-curtain effect," *Optica* (2016).
- E. Edrei and G. Scarcelli, "Memory-effect based deconvolution microscopy for super-resolution imaging through scattering media," *Sci. Reports* (2016).
- M. Hofer, C. Soeller, S. Brasselet, and J. Bertolotti, "Wide field fluorescence epi-microscopy behind a scattering medium enabled by speckle correlations," *Opt. Express* (2018).
- T. Wu, J. Dong, X. Shao, and S. Gigan, "Imaging through a thin scattering layer and jointly retrieving the point-spread-function using phase-diversity," *Opt. Express* (2017).
- T. Wu, J. Dong, and S. Gigan, "Non-invasive single-shot recovery of a point-spread function of a memory effect based scattering imaging system," *Opt. Lett.* (2020).
- X. Wang, X. Jin, and J. Li, "Blind position detection for large field-of-view scattering imaging," *Photon. Res.* (2020).
- J. Chang and G. Wetzstein, "Single-shot speckle correlation fluorescence microscopy in thick scattering tissue with image reconstruction priors," *J. Biophotonics* (2018).
- M. Alterman, C. Bar, I. Gkioulekas, and A. Levin, "Imaging with local speckle intensity correlations: theory and practice," *ACM TOG* (2021).
- M. Zhou, A. Pan, R. Li, Y. Liang, J. Min, T. Peng, C. Bai, and B. Yao, "Retrieval of non-sparse object through scattering media beyond the memory effect," *J. Opt.* (2020).
- D. F. Gardner, S. Divitt, and A. T. Watnik, "Ptychographic imaging of incoherently illuminated extended objects using speckle correlations," *Appl. Opt.* (2019).
- G. Li, Y. Wanqin, W. Haichao, and G. Situ, "Image transmission through scattering media using ptychographic iterative engine," *Appl. Sci.* (2019).
- L. Li, X. Wen, R. Song, J.-T. Jiang, H.-L. Zhang, X.-B. Liu, and L. Wei, "Imaging correlography using ptychography," *Appl. Sci.* (2019).
- N. Shekel and O. Katz, "Using fiber-bending-generated speckles for improved working distance and background rejection in lensless microendoscopy," *Opt. Lett.* **45**, 4288–4291 (2020).
- A. Boniface, J. Dong, and S. Gigan, "Non-invasive focusing and imaging in scattering media with a fluorescence-based transmission matrix," *Nat. Commun.* (2020).
- L. Zhu, F. Soldevila, C. Moretti, A. d'Arco, A. Boniface, X. Shao, H. B. de Aguiar, and S. Gigan, "Large field-of-view non-invasive imaging through scattering layers using fluctuating random illumination," *arXiv preprint arXiv:2017.08158* (2021).
- A. Boniface, B. Blochet, J. Dong, and S. Gigan, "Noninvasive light focusing in scattering media using speckle variance optimization," *Optica* (2019).
- D. Aizik, I. Gkioulekas, and A. Levin, "Fluorescent wavefront shaping using incoherent iterative phase conjugation," *arXiv preprint* (2022).
- G. Osnabrugge, R. Horstmeyer, I. N. Papadopoulos, B. Judkewitz, and I. M. Vellekoop, "Generalized optical memory effect," *Optica* (2017).
- C. Bar, M. Alterman, I. Gkioulekas, and A. Levin, "Single scattering modeling of speckle correlation," in *ICCP*, (2021).
- M. Riley and M. Gusinow, "Laser beam divergence utilizing a lateral shearing interferometer," *Appl. Opt.* **16**, 2753–2756 (1977).
- J. M. Rodenburg, A. C. Hurst, A. G. Cullis, B. R. Dobson, F. Pfeiffer, O. Bunk, C. David, K. Jefimovs, and I. Johnson, "Hard-x-ray lensless imaging of extended objects," *Phys. Rev. Lett.* **98** (2007).
- D. P. Kingma and J. Ba, "Adam: A method for stochastic optimization," *ICLR* (2015).
- P. Hariharan, B. Oreb, and T. Eiju, "Digital phase-shifting interferometry: a simple error-compensating phase calculation algorithm," *Appl. Opt.* **26**, 2504–2506 (1987).
- S. Schott, J. Bertolotti, J.-F. Léger, L. Bourdieu, and S. Gigan, "Characterization of the angular memory effect of scattered light in biological tissues," *Opt. express* **23**, 13505–13516 (2015).
- A. Boniface, B. Blochet, J. Dong, and S. Gigan, "Noninvasive light focusing in scattering media using speckle variance optimization," *Optica* **6**, 1381–1385 (2019).

Enhancing Speckle Statistics for Imaging Inside Scattering Media

Supplementary Appendix

A. APPENDIX

A. Analyzing correlation properties in translating interferometry measurements

In this section, we formulate and prove a few properties of translating interferometry modulations mentioned in the main paper.

Throughout this derivation, we assume that different pixels \mathbf{v} in a speckle pattern $u^i(\mathbf{v})$ arising from one source are independent random variables. In practice, depending on magnification, the grain of speckle features on the sensor may be wider than a single pixel. This would imply some scaling adjustments in the exact formulas, which we neglect here. We also ignore small dependencies introduced by the low pass filtering of Eq. (4) and treat entries of $S^i(\mathbf{v})$ as independent random variables.

Also, in the following derivations expectations are taken with respect to multiple realization of scattering volumes with the same material parameters. For example, the notation $\mathbb{E}[\mathcal{C}^i(\Delta)]$ refers to the following. Suppose we had N different tissue layers of the same type, and we place behind each layer fluorescent sources at the exact same layout. We image N different speckle images and compute N different auto-correlations $\mathcal{C}^i(\Delta)$. For large N values averaging these auto-correlations provides the idealized expected speckle-auto correlation for that source layout, denoted $\mathbb{E}[\mathcal{C}^i(\Delta)]$. Similarly $\text{Var}[\mathcal{C}^i(\Delta)]$ denotes the variance we expect to see in such auto-correlation. As correlation is computed from a finite number of speckle pixels the correlation is never zero even in displacements Δ that do not correspond to an actual illuminator displacement. To define variance mathematically one needs to compute such auto-correlations from N different speckle images of the same illuminator layout. In practice for the evaluation in Fig. 3 we only compute the expectation and variance between different Δ displacements of the auto-correlation of a single tissue sample.

Claim 1 We define correlation contrast

$$\Theta(\mathcal{C}^{I_1, \dots, I_T}) = \frac{\frac{1}{|\Gamma_\Delta|} \sum_{\Delta \in \Gamma_\Delta} \mathbb{E}[\mathcal{C}^{I_1, \dots, I_T}(\Delta)]^2}{\frac{1}{|\Gamma_\Delta^c|} \sum_{\Delta \in \Gamma_\Delta^c} \text{Var}[\mathcal{C}^{I_1, \dots, I_T}(\Delta)]} \quad (\text{S1})$$

If the speckle patterns S_t^0 are uncorrelated with each other for different t values, then the correlation contrast increases linearly with the number of measurements T .

Proof: The claim is based on the observation that for displacements $\Delta \in \Gamma_\Delta$ that correspond to an actual illuminator's displacement, $\mathbb{E}[\mathcal{C}^{I_1, \dots, I_T}(\Delta)]$ is a positive quantity, while for $\Delta \in \Gamma_\Delta^c$, which do not correspond to a displacement between two illuminators, no correlation exists and in expectation $\mathbb{E}[\mathcal{C}^{I_1, \dots, I_T}(\Delta)] = 0$.

With this understanding, we note that expectation is linear and hence recalling the definition of $\mathcal{C}^{I_1, \dots, I_T}(\Delta)$ in Eq. (10) of the main paper, the numerator of Eq. (S1) is independent of the number of measurements T :

$$\mathbb{E}[\mathcal{C}^{I_1, \dots, I_T}(\Delta)] = \frac{1}{T} \sum_t \mathbb{E}[\mathcal{C}^{I_t}(\Delta)] = \mathbb{E}[\mathcal{C}^{I_1}(\Delta)]. \quad (\text{S2})$$

We now move to express the denominator. First, we note that as our signal I_1, \dots, I_T are zero mean as defined in Eq. (14).

$$\text{Var}[\mathcal{C}^{I_1, \dots, I_T}(\Delta)] = \mathbb{E}\left[|\mathcal{C}^{I_1, \dots, I_T}(\Delta)|^2\right] \quad (\text{S3})$$

Thus, we expand the second moment below. Using again the definition of the average correlation in Eq. (10) of the main paper, we express:

$$\mathbb{E}\left[|\mathcal{C}^{I_1, \dots, I_T}(\Delta)|^2\right] = \frac{1}{T^2} \sum_{(t_1, t_2)} \mathbb{E}[\mathcal{C}^{I_{t_1}}(\Delta) \cdot \mathcal{C}^{I_{t_2}}(\Delta)^*] \quad (\text{S4})$$

$$= \frac{1}{T^2} \sum_t \mathbb{E}[\mathcal{C}^{I_t}(\Delta) \cdot \mathcal{C}^{I_t}(\Delta)^*] \quad (\text{S5})$$

$$+ \frac{1}{T^2} \sum_{(t_1 \neq t_2)} \mathbb{E}[\mathcal{C}^{I_{t_1}}(\Delta)] \cdot \mathbb{E}[\mathcal{C}^{I_{t_2}}(\Delta)]^* \quad (\text{S6})$$

$$= \frac{1}{T^2} \sum_t \mathbb{E}[|\mathcal{C}^{I_t}(\Delta)|^2] \quad (\text{S7})$$

$$= \frac{1}{T} \mathbb{E}[|\mathcal{C}^{I_1}(\Delta)|^2] \quad (\text{S8})$$

where Eq. (S6) follows from the assumption that for $t_1 \neq t_2$ the speckles $S_{t_1}^0, S_{t_2}^0$ are uncorrelated with each other, and Eq. (S7) from the fact that for displacements $\Delta \in \Gamma_\Delta^c$ the correlation has zero expectation.

From Eq. (S8), we conclude that as we increase the number of measurements the denominator scales as $1/T$. As a result the correlation contrast in Eq. (S1) scales linearly with T . ■

Below, we show that unlike the random modulation of Eq. (12), the translating interferometry measurements of Eq. (13) do not reduce the correlation.

Claim 2 For displacements in the order of a few speckle grains, the correlation between translating interferometry signals S_t^1, S_t^2 produced by different illuminators $\mathbf{i}^1, \mathbf{i}^2$ is approximately the same as the correlation of the original speckle intensity images.

Proof: As we filter the intensity images to have zero mean, the expected correlation becomes the intensity covariance C_I defined in [11]:

$$C_I(|u^{\mathbf{i}^1}(\mathbf{v})|^2, |u^{\mathbf{i}^2}(\mathbf{v} + \Delta)|^2) \quad (\text{S9})$$

$$\equiv \mathbb{E}[|u^{\mathbf{i}^1}(\mathbf{v})|^2 |u^{\mathbf{i}^2}(\mathbf{v} + \Delta)|^2] - \mathbb{E}[|u^{\mathbf{i}^1}(\mathbf{v})|^2] \mathbb{E}[|u^{\mathbf{i}^2}(\mathbf{v} + \Delta)|^2] \quad (\text{S10})$$

Where the expectation is taken over multiple tissue layers of the same type. Classical statistics results state that the covariance between intensities is the square of the covariance between the complex zero mean fields u . Thus, the above definition can be further simplified to:

$$C_I(|u^{\mathbf{i}^1}(\mathbf{v})|^2, |u^{\mathbf{i}^2}(\mathbf{v} + \Delta)|^2) = |\mathbb{E}[u^{\mathbf{i}^1}(\mathbf{v})u^{\mathbf{i}^2}(\mathbf{v} + \Delta)^*]|^2 \quad (\text{S11})$$

On the other hand, we consider the correlation between translating interferometry signals:

$$C_I(S_t^i(\mathbf{v}), S_t^i(\mathbf{v} + \Delta)) \quad (\text{S12})$$

$$= \mathbb{E} [S_t^i(\mathbf{v})S_t^i(\mathbf{v} + \Delta)] - \mathbb{E} [S_t^i(\mathbf{v})] \mathbb{E} [S_t^i(\mathbf{v} + \Delta)] \quad (\text{S13})$$

As before, the second term vanishes as in translating interferometry, $S_t^i(\mathbf{v})$ is a zero mean signal. Also as we assume that different pixels of a speckle pattern are independent, we can express:

$$\mathbb{E} [S_t^i(\mathbf{v})S_t^i(\mathbf{v} + \Delta)] \quad (\text{S14})$$

$$= \mathbb{E} [u^i(\mathbf{v})u^i(\mathbf{v} + \mathbf{d}_t)^* u^i(\mathbf{v} + \Delta)^* u^i(\mathbf{v} + \Delta + \mathbf{d}_t)] \quad (\text{S15})$$

$$= \mathbb{E} [u^i(\mathbf{v})u^i(\mathbf{v} + \Delta)^*] \mathbb{E} [u^i(\mathbf{v} + \mathbf{d}_t)u^i(\mathbf{v} + \Delta + \mathbf{d}_t)^*].$$

Now we assume the displacement \mathbf{d}_t is modest enough so that the correlation at pixel \mathbf{v} and the correlation at a small displacement, at pixel $\mathbf{v} + \mathbf{d}_t$ is similar, so that

$$\mathbb{E} [u^i(\mathbf{v})u^i(\mathbf{v} + \Delta)^*] \approx \mathbb{E} [u^i(\mathbf{v} + \mathbf{d}_t)u^i(\mathbf{v} + \Delta + \mathbf{d}_t)^*]. \quad (\text{S16})$$

Put all together, we can derive

$$C_I(S_t^i(\mathbf{v}), S_t^i(\mathbf{v} + \Delta)) \approx \left| \mathbb{E} [u^i(\mathbf{v})u^i(\mathbf{v} + \Delta)^*] \right|^2 \quad (\text{S17})$$

$$= C_I(|u^i(\mathbf{v})|^2, |u^i(\mathbf{v} + \Delta)|^2) \quad (\text{S18})$$

We now show that despite the fact that we capture multiple images through the same tissue layer and our measurements are not independent, they are still uncorrelated which is enough to reduce the noise of the speckle auto-correlation we evaluate.

Claim 3 For displacements $\mathbf{d}_{t_1}, \mathbf{d}_{t_2}$ whose distance $\|\mathbf{d}_{t_1} - \mathbf{d}_{t_2}\|$ is larger than the speckle grain, the signals $S_{t_1}^i, S_{t_2}^i$ are uncorrelated, so that

$$\mathbb{E} [S_{t_1}^i \cdot S_{t_2}^{i*}] - \mathbb{E} [S_{t_1}^i] \cdot \mathbb{E} [S_{t_2}^i]^* = 0 \quad (\text{S19})$$

Proof: Our derivation is based on the assumption that the speckle fields u^i have zero means, and the speckle values in different sensor positions \mathbf{v} are independent random variables. For a non zero displacement \mathbf{d}_t we get

$$\begin{aligned} \mathbb{E} [S_t^i] &= \mathbb{E} [u^i(\mathbf{v})u^i(\mathbf{v} + \mathbf{d}_t)] \\ &= \mathbb{E} [u^i(\mathbf{v})] \mathbb{E} [u^i(\mathbf{v} + \mathbf{d}_t)] = 0. \end{aligned} \quad (\text{S20})$$

In a similar way

$$\mathbb{E} [S_{t_1}^i S_{t_2}^{i*}] = \mathbb{E} [u^i(\mathbf{v})u^i(\mathbf{v} + \mathbf{d}_{t_1})^* u^i(\mathbf{v})^* u^i(\mathbf{v} + \mathbf{d}_{t_2})] \quad (\text{S21})$$

$$= \mathbb{E} [|u^i(\mathbf{v})|^2 u^i(\mathbf{v} + \mathbf{d}_{t_1})^* u^i(\mathbf{v} + \mathbf{d}_{t_2})] \quad (\text{S22})$$

$$= \mathbb{E} [|u^i(\mathbf{v})|^2] \mathbb{E} [u^i(\mathbf{v} + \mathbf{d}_{t_1})^*] \mathbb{E} [u^i(\mathbf{v} + \mathbf{d}_{t_2})] \quad (\text{S23})$$

$$= 0. \quad (\text{S24})$$

Where Eq. (S23) follows again from the assumption that speckle at different pixel positions are independent. Eq. (S20) and Eq. (S24) prove the desired Eq. (S19). ■

We now move to study the relationship between the correlation we can measure from translating interferometry to the actual correlation of the latent pattern.

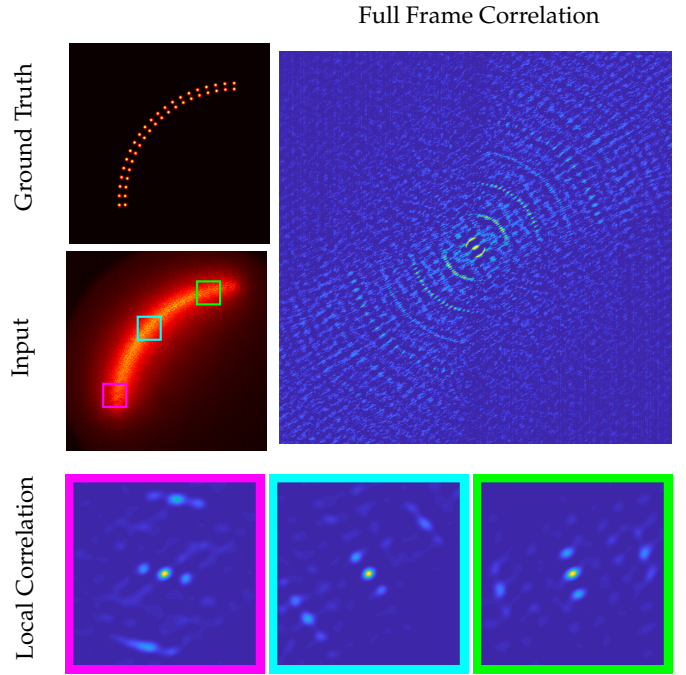


Fig. S1. Local versus global auto-correlation. The orientation of the auto-correlation evaluated in three different local windows of the image matches the orientation of the arc in the corresponding region of the latent image. By contrast, the auto-correlation of the full frame is much noisier, and decays for large displacements due to limited ME.

Claim 4 For speckle fields $u^i(\mathbf{v}), u^i(\mathbf{v})$ satisfying the tilt shift relationship of Eq. (1), the translating interferometry measurements $S_t^i(\mathbf{v})$ and $S_t^i(\mathbf{v})$ defined in Eq. (13) are shifted versions of each other, times a globally constant phasor, which is independent of pixel position \mathbf{v} . This is expressed by the relationship:

$$S_t^i(\mathbf{v}) \approx S_t^i(\mathbf{v} + \Delta) e^{-jk\alpha \langle \Delta, \mathbf{d}_t \rangle}, \quad (\text{S25})$$

with $\Delta = \mathbf{i}^2 - \mathbf{i}^1$.

Proof: From Eq. (1), we have $u^i(\mathbf{v}) \approx e^{jk\alpha \langle \Delta, \tau \rangle} u^i(\mathbf{v} + \Delta)$, with $\tau = \mathbf{v} - \mathbf{i}^1$. Substituting into Eq. (13) we have,

$$\begin{aligned} S_t^i(\mathbf{v}) &= u^i(\mathbf{v})u^i(\mathbf{v} + \mathbf{d}_t)^* \\ &\approx e^{jk\alpha \langle \Delta, \tau \rangle} u^i(\mathbf{v} + \Delta) e^{-jk\alpha \langle \Delta, \tau + \mathbf{d}_t \rangle} u^i(\mathbf{v} + \Delta + \mathbf{d}_t)^* \\ &= e^{-jk\alpha \langle \Delta, \mathbf{d}_t \rangle} u^i(\mathbf{v} + \Delta) u^i(\mathbf{v} + \Delta + \mathbf{d}_t)^* \\ &= e^{-jk\alpha \langle \Delta, \mathbf{d}_t \rangle} S_t^i(\mathbf{v} + \Delta) \end{aligned}$$

With all the above claims we are now ready to prove our main result and show that the global phasor of the previous claim translates into a phase ramp in the auto-correlation.

Claim 5 Using the translating interferometry measurements of Eq. (13), the speckle auto-correlation $\mathcal{C}^I = I_t \star I_t$ is equivalent to the auto-correlation of the latent pattern $\mathcal{C}^O = O \star O$, times a phase ramp correction

$$\mathcal{C}^I(\Delta) \approx \mathcal{C}^O(\Delta) e^{-jk\alpha \langle \Delta, \mathbf{d}_t \rangle}. \quad (\text{S26})$$

Proof: Using Claim 4 for the specific case $\mathbf{i}^1 = \mathbf{i}^n$ and $\mathbf{i}^2 = \mathbf{0}$ we get $S_t^{\mathbf{i}^n}(\mathbf{v}) \approx S_t^{\mathbf{0}}(\mathbf{v} + \mathbf{i}^n) e^{-jk\alpha \langle \mathbf{i}^n, \mathbf{d}_t \rangle}$. Summing over all sources $S_t^{\mathbf{i}^n}(\mathbf{v})$ we have

$$I_t(\mathbf{v}) \approx S_t^{\mathbf{0}} * \tilde{O},$$

with \tilde{O}

$$\tilde{O}(\mathbf{v}) = O(\mathbf{v}) e^{-jk\alpha \langle \mathbf{v}, \mathbf{d}_t \rangle}. \quad (\text{S27})$$

This is due to the fact that O is non zero only at positions $\mathbf{v} = \mathbf{i}^n$ for one of the sources, so effectively \tilde{O} has for each sensor position \mathbf{i}^n the global phasor of Eq. (S25). As in the standard derivation of the speckle auto-correlation we assume $S_t^{\mathbf{0}} * S_t^{\mathbf{0}} = \delta$, and hence

$$I_t * I_t \approx \tilde{O} * \tilde{O}. \quad (\text{S28})$$

or equivalently

$$\mathcal{C}^{I_t}(\Delta) \approx \mathcal{C}^{\tilde{O}}(\Delta). \quad (\text{S29})$$

Hence we are left with the need of computing $\mathcal{C}^{\tilde{O}}(\Delta)$. We note that by the Wiener-Khinchin theorem, $\mathcal{C}^{\tilde{O}}(\Delta)$ is the inverse Fourier transform of $|\mathcal{F}(\tilde{O})|^2$. However as \tilde{O} is obtained by multiplying O with a phase ramp (see Eq. (S27)), their Fourier transforms are related via a shift:

$$\mathcal{F}(\tilde{O})(\omega) = \mathcal{F}(O)(\omega + \alpha \mathbf{d}_t). \quad (\text{S30})$$

The shift relation holds also for their absolute values

$$|\mathcal{F}(\tilde{O})(\omega)|^2 = |\mathcal{F}(O)(\omega + \alpha \mathbf{d}_t)|^2 \quad (\text{S31})$$

Hence $\mathcal{C}^{\tilde{O}}(\Delta)$ and $\mathcal{C}^O(\Delta)$ are related via a tilt:

$$\mathcal{C}^{\tilde{O}}(\Delta) = \mathcal{C}^O(\Delta) e^{-jk\alpha \langle \Delta, \mathbf{d}_t \rangle}. \quad (\text{S32})$$

Substituting Eq. (S32) in Eq. (S29) proves the desired Eq. (S26). \blacksquare

B. Optimizing using local support

For sources located inside the scattering medium, speckle patterns emerging from a single source have local support and do not spread over the entire sensor. To take advantage of this property, [11] suggest matching the local speckle correlations in the image, rather than the full-frame auto-correlation. We review this algorithm below.

For motivation, consider Fig. S1 that we re-plot from [11]. It visualizes speckles produced by latent incoherent illuminators in a double arc layout. Computing auto-correlation at small subwindows of the speckle image reveals the local orientation of the arc in the latent image. By contrast, when computing the auto-correlation of the full frame, the correlation is considerably noisier even for small displacements. Correlations between far illuminators are even harder to detect due to the fact that the ME range is limited and for large displacements Δ the desired correlation (see Eq. (1)) is very weak.

The optimization algorithm takes as input two threshold parameters T_τ, T_Δ . It assumes that speckles from one illuminator are spread over pixels in a window of size T_τ around it, and that ME correlation holds for displacements $|\Delta| < T_\Delta$. The thresholds T_τ, T_Δ are free parameters that can be fine-tuned to improve reconstruction quality, and [11] show that performance are not too sensitive to their exact values. The algorithm offers improved performance compared to the baseline full-frame auto-correlation algorithm in situations where $T_\tau < T_\Delta$, namely when the support from one illuminator is lower than the ME range. For

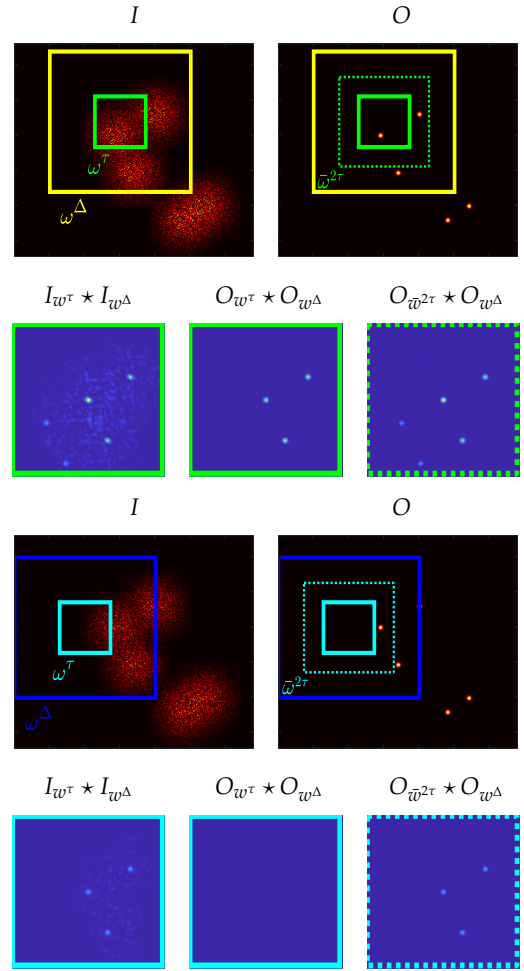


Fig. S2. Local window selection for optimization. We consider local subwindows w^τ (light green and cyan frames) whose support is equivalent to the speckle support size. Each such window is correlated with a wider window w^Δ (yellow and blue frames) around it, whose support is equivalent to the ME range. As speckle inside window w^τ can arise from a source outside w^τ , $O_{w^\tau} * O_{w^\Delta}$ may not match $I_{w^\tau} * I_{w^\Delta}$. To overcome this, we use an extended non-binary sub-window $\tilde{w}^{2\tau} = w^\tau * w^\tau$ for O , whose support is indicated by dashed lines.

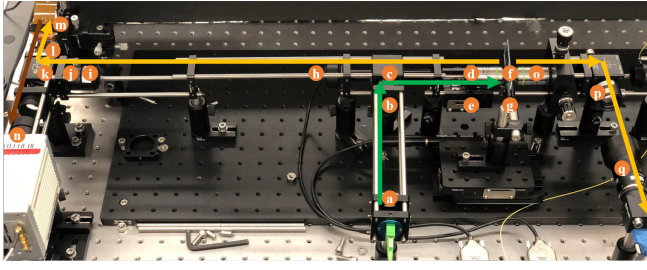
thick scattering slices, where high-order scattering is dominant, this relationship does not hold and the approach reduces to the baseline full-frame auto-correlation algorithm.

The algorithm searches for a latent image O such that the auto-correlation in its local windows will match the auto-correlation in the local windows of the input image I . We define w^Δ and w^τ to be binary windows with support T_Δ, T_τ , respectively, and $\tilde{w}^{2\tau} = w^\tau * w^\tau$ —note that, from its definition, $\tilde{w}^{2\tau}$ is non-binary. Then, we recover O by solving the optimization problem:

$$\min_O \sum_p \left\| \frac{1}{T} \sum_t e^{jk\alpha \langle \Delta, \mathbf{d}_t \rangle} \cdot I_{t, w_p^\tau} * I_{t, w_p^\Delta} - O_{\tilde{w}_p^{2\tau}} * O_{w_p^\Delta} \right\|^2, \quad (\text{S33})$$

where $I_{t, w_p^\tau}, I_{t, w_p^\Delta}, O_{\tilde{w}_p^{2\tau}}, O_{w_p^\Delta}$ denote windows of a given size cropped from the input and latent images, centered around the p -th pixel.

Eq. (S33) uses windows of three different sizes, and we use Fig. S2 to visualize their different roles: Each w_p^τ is a small win-



- | | |
|--|---|
| Ⓐ Fibered laser (Coherent Sapphire, $\lambda = 530\text{nm}$) | Ⓚ Polarized beam splitter (Thorlabs PBS251) |
| Ⓑ Lens ($f = 200\text{mm}$) | Ⓛ Quarter wave plate (Thorlabs AQPW10M-580) |
| Ⓒ Dichromatic mirror (Omega 560DRLP) | Ⓜ SLM (Holoeye LETO) |
| Ⓓ Objective lens (Olympus RMS 20x) | Ⓝ Main camera (Hamamatsu ORCA-Flash4.0 LT+) |
| Ⓔ Z translation stage (Thorlabs XR25P, Z825B) | Ⓗ Objective lens (Olympus RMS 20x) |
| Ⓕ Tissue and fluorescent beads | Ⓘ Bandpass filter (Omega 575DF10, 577BP10) |
| Ⓖ Z translation stage (Thorlabs CT1, Z825B) | Ⓣ Validation camera (FLIR GS3-U3-28S5M-C) |
| Ⓒ Lens ($f = 200\text{mm}$) | — Excitation laser |
| Ⓙ Bandpass filter (Edmund 87-752, 65-161) | — Emitted fluorescent light |
| Ⓛ Lens ($f = 100\text{mm}$) | — Modulated fluorescent light |

Fig. S3. Hardware prototype. Image of our prototype, analogous to the schematic in Fig. 4.

dow around pixel p whose support is equivalent to the expected support size of the speckle pattern due to a single illuminator. w_p^Δ is a larger window around the same pixel, corresponding to the maximal displacement T_Δ for which we expect to find correlation, as dictated by the ME range.

We note, additionally, that the window cropped from O should be wider than that from I . This is because speckle at a certain pixel can arise from an illuminator within a window around it. For example, in Fig. S2, no illuminator is located inside the cyan subwindow of O , but part of the speckle pattern of a neighboring source is leaking into the corresponding cyan subwindow of I . As a result $O_{w_p^\tau} \star O_{w_p^\Delta}$ is a zero image, even though $I_{w_p^\tau} \star I_{w_p^\Delta}$ detects three impulses. It is easy to prove that this can be addressed using the larger, non-binary window $\tilde{w}^{2\tau}$ in the latent image, indicated in Fig. S2 using dashed lines: in this case, $O_{\tilde{w}^{2\tau}} \star O_{w_p^\Delta}$ correctly detects the same three impulses as $I_{w_p^\tau} \star I_{w_p^\Delta}$.

The motivation for the cost of Eq. (S33) is that, even if two illuminators in the latent pattern O are at a distance larger than the ME range T_Δ , they can be recovered if there exists a sequence of illuminators between them, where each two consecutive illuminators in the sequence are separated by a distance smaller than T_Δ . For example, in Fig. S2, the illuminators outside the yellow and cyan w^Δ windows are recovered thanks to the intermediate illuminators.

The optimization problem in Eq. (S33) is no longer a phase retrieval problem as in standard full-frame auto-correlation algorithms. We minimize it using the ADAM gradient-based optimizer [25]. Gradient evaluation is described in [11], and reduces to a sequence of convolution operations that can be performed efficiently, e.g., using a GPU based fast Fourier transform. For initialization, we set the latent image to random noise; we have observed empirically that the optimization is fairly insensitive to initialization. Finally, we note that even though we could place a window w_p around every pixel of I , the empirical correlation is insensitive to small displacements of the central pixel p . Therefore, in practice, we consider windows only at strides $T_\tau/2$, which helps reduce computational complexity.

We note that the optimization problem of Eq. (S33) is similar

to ptychography algorithms [24]. However, we emphasize that previous ptychographic approaches for extending the ME range recover the latent illuminators from *multiple* image measurements, captured by sequentially exciting different areas on the scattering sample [12–16]. By contrast, our algorithm recovers the latent illuminators from a fixed number of full-frame shots.

C. Interferometric measurements

While most of our setup is similar to the one used by [11], we use an SLM (Holoeye LETO) in the Fourier plane of the imaging arm, which we use to modulate the scattered light. We visualize the hardware schematic in Fig. 4 and its image in Fig. S3. To capture interferometric measurements, we use a polarizing beamsplitter to horizontally polarize the wave, followed by a quarter waveplate at an angle of 45° to induce a $\pi/2$ phase delay along one of the axis to produce a circularly polarized light. The SLM only modulates the polarization state along its fast axis, which is horizontal, and its slow axis is reflected without any modulation. The light reflected off the SLM is sent again through quarter waveplate, which adds another $\pi/2$ phase shift that makes the light linearly polarized again, but in a vertical direction; finally, the polarizing beamsplitter interferes the modulated and unmodulated waves.

To capture the translating interferometry measurements of Eq. (13), we place on the SLM a phase ramp whose frequency and orientation matches the translation \mathbf{d}_t we want to implement. We capture $K = 3$ images of this phase ramp plus a global phasor $\phi_k \in \{0, \frac{\pi}{3}, \frac{2\pi}{3}\}$. Since the SLM modulates only part of the wave, we obtain the measurement

$$\hat{S}_t^{i^n, k} = \left| u^{i^n}(\mathbf{v}) + e^{j\phi_k} u^{i^n}(\mathbf{v} + \mathbf{d}_t) \right|^2, \quad (\text{S34})$$

where k index the phase shift, n index the fluorescent source, and t index the translation \mathbf{d}_t of the current measurement. Using phase-shifting interferometry [26], we can extract the interference signal desired in Eq. (13) as:

$$S_t^{i^n} = \sum_k e^{j\phi_k} \left| u^{i^n}(\mathbf{v}) + e^{j\phi_k} u^{i^n}(\mathbf{v} + \mathbf{d}_t) \right|^2 = u^{i^n}(\mathbf{v}) u^{i^n}(\mathbf{v} + \mathbf{d}_t)^*, \quad (\text{S35})$$

In the presence of multiple incoherent sources, emission from different sources do not interfere. Thus, the measured intensity in each shot is equivalent to $\hat{I}_t^k = \sum_n \hat{S}_t^{i^n, k}$. With the phase shifting interferometry in Eq. (S35) we extract $I_t = \sum_n S_t^{i^n}$.

D. Setup for the spatial incoherent target

We wanted to test our algorithm on incoherent illumination layout of arbitrary complexity, as in Fig. 6. Thus, in addition to fluorescent beads we created incoherent illumination patterns with a shifting laser setup using the setup illustrated in Fig. S4. For this, we imaged the diffused output of a fibered laser (635nm) to generate a point focused exactly at the back of the tissue (we use the validation camera for accurate focusing). The main camera at the other side of the tissue captured the intensity scattered from this spot. We then translate the fiber output on a programmable xy stage to generate spots at other positions behind the tissue. We capture a sequence of images at each source position and sum their *intensities*, thus simulating incoherent summation from multiple sources. This setup allows us to control the layout and complexity of the sources, which is useful for analyzing our algorithm with patterns of controlled complexities as in Fig. 2 and replicating the same layout behind multiple tissue slices as in Fig. 3 and S8.

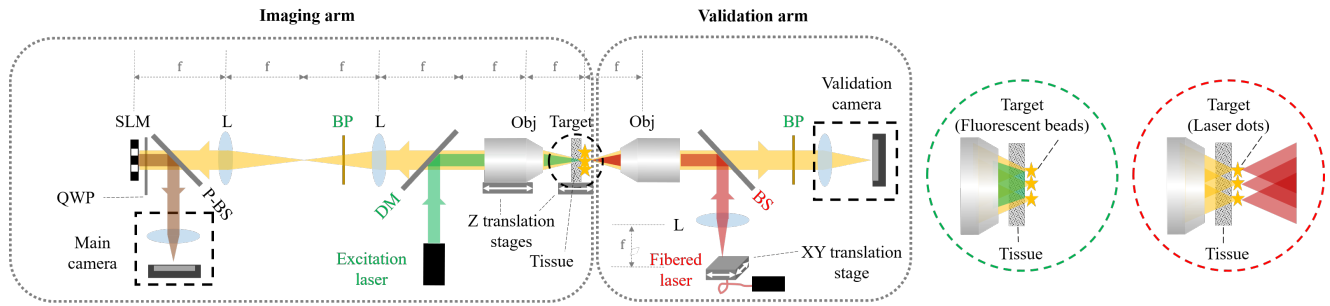


Fig. S4. Full experiment setup combining fluorescent beads with a shifting laser. We add to the setup in Fig. 4 a fibered laser source. The diffused fibered output is imaged using a tube lens and objective to generate a source exactly at the back plane of a tissue layer. The laser light is scattered through the tissue and the speckle pattern it generates is imaged by the main camera from the other side of the tissue. We mount a fibered laser on a 2D translation stage so we can create programmable patterns.

E. Additional results

In Fig. S5 we show additional reconstruction results using fluorescent bead targets as well as shifting laser dots targets. Both used tissue slices of thickness around $\sim 150\mu\text{m}$. In Fig. S9 we use fluorescent beads behind a parafilm phantom, see characterization in Sec. A.H.

F. Translating interferometry without phase correction

As noted in Claim 4, when using our translating interferometry, we need a phase ramp correction to the auto-correlation of speckles. To support the claim, we compare results with and without the correction. In Fig. S6, we show the auto-correlation obtained by averaging translating interferometry measurements I_t (Eq. (14)) with and without the phase ramp correction of Eq. (16). The phase correction further improves the contrast, especially at larger displacements Δ . In Fig. S7 we further show the reconstruction result of translating interferometry with and without the phase ramp correction. If the phase correction is not used not all the sources are recovered.

G. Tissue thickness

In Fig. S8 we used the scanning laser setup to create the same illumination layout behind different tissue slices. This allows us to compare reconstructions through different tissue thicknesses. For the thickest layer the reconstruction failed.

As discussed in [11], thicker tissue leads to larger speckle spread and weaker memory effect correlation. We used the fact that the scanning laser setup captures speckle patterns by different point sources separately, to evaluate statistical correlation through the different tissue layers. In the top part of Fig. S8 we plot the correlation we measured between speckle patterns generated by different sources, as a function of the displacement between the sources. As expected, as the tissue thickness increases the correlation decays faster as a function of displacement, explaining the reconstruction failure in the lowest row.

These results demonstrate the limitation of our method: while we can improve correlation contrast, our approach is still based on the existence of some memory effect correlation and will fail when this correlation is too weak.

H. Tissue preparation and characterization

Most results in this paper used chicken breast tissue as a scattering material. We cut thin slice from thawed chicken breast. To keep the tissue fresh, we did the fluorescent imaging experiment within 3 hours. The scanning laser targets require longer

capture. To keep freshness we squeeze the tissue between two cover glasses and seal them using nail polish.

As stated in [27], chicken breast tissue has an anisotropy parameter $g = 0.965$ and a mean free path (MFP) around $43.7\mu\text{m}$. However, these parameters may vary significantly between different tissue slices.

For a better characterization, we also use a parafilm phantom. This was calibrated in [28], reporting an anisotropy parameter $g = 0.77$ and a MFP around $170\mu\text{m}$. We imaged through one parafilm layer whose thickness is about $120\mu\text{m}$. Results for this phantom are demonstrated in Fig. S9. Note that while the parafilm has a longer MFP, it also has a smaller anisotropy factor and in practice the speckle spreads of both parafilm and chicken breast are comparable.

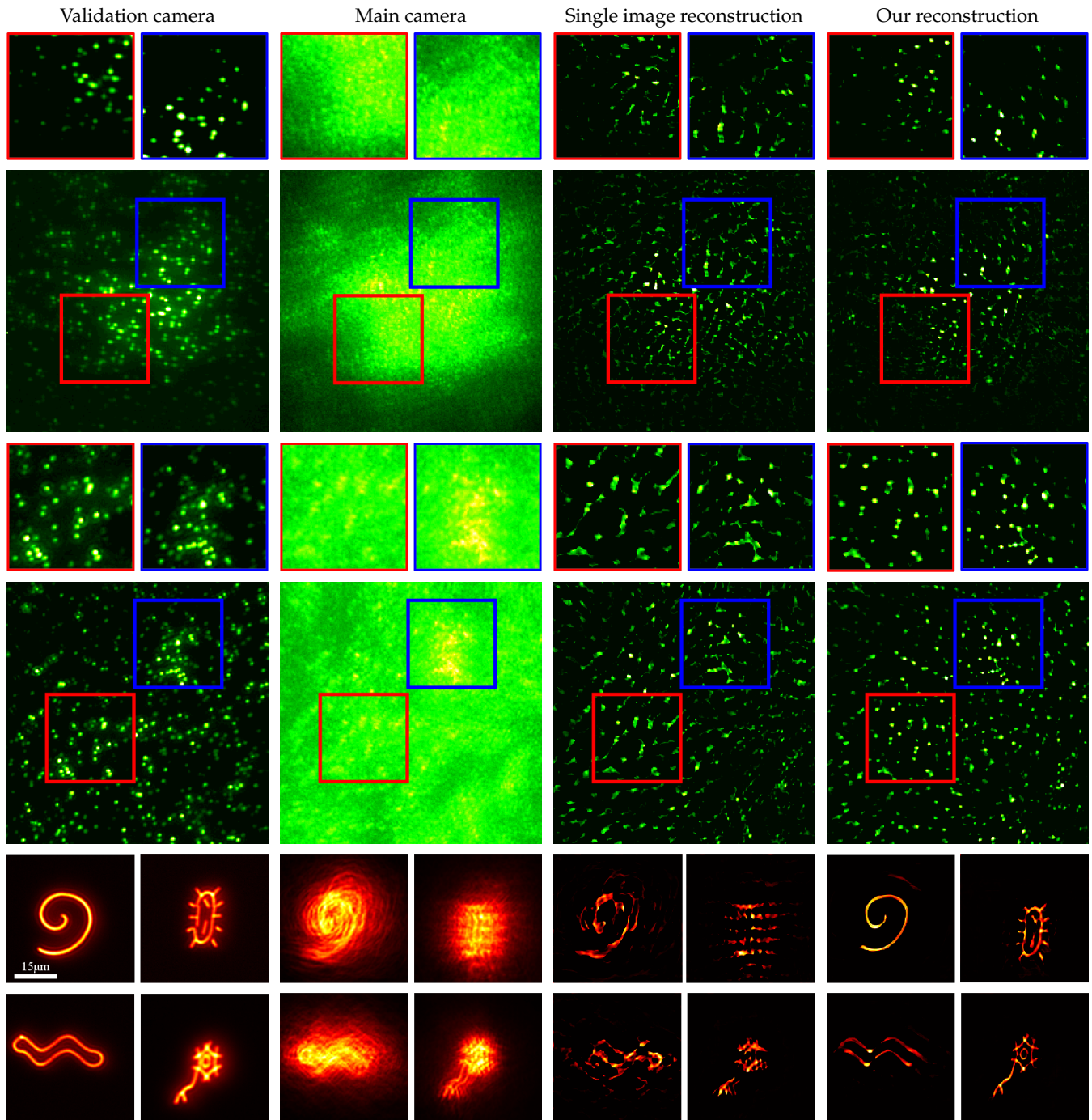


Fig. S5. Additional reconstruction results. Top panel: results on a fluorescent bead image. Lower panel: results using shifting laser inputs. Both inputs were images through $\sim 150\mu\text{m}$ -thick tissue slices

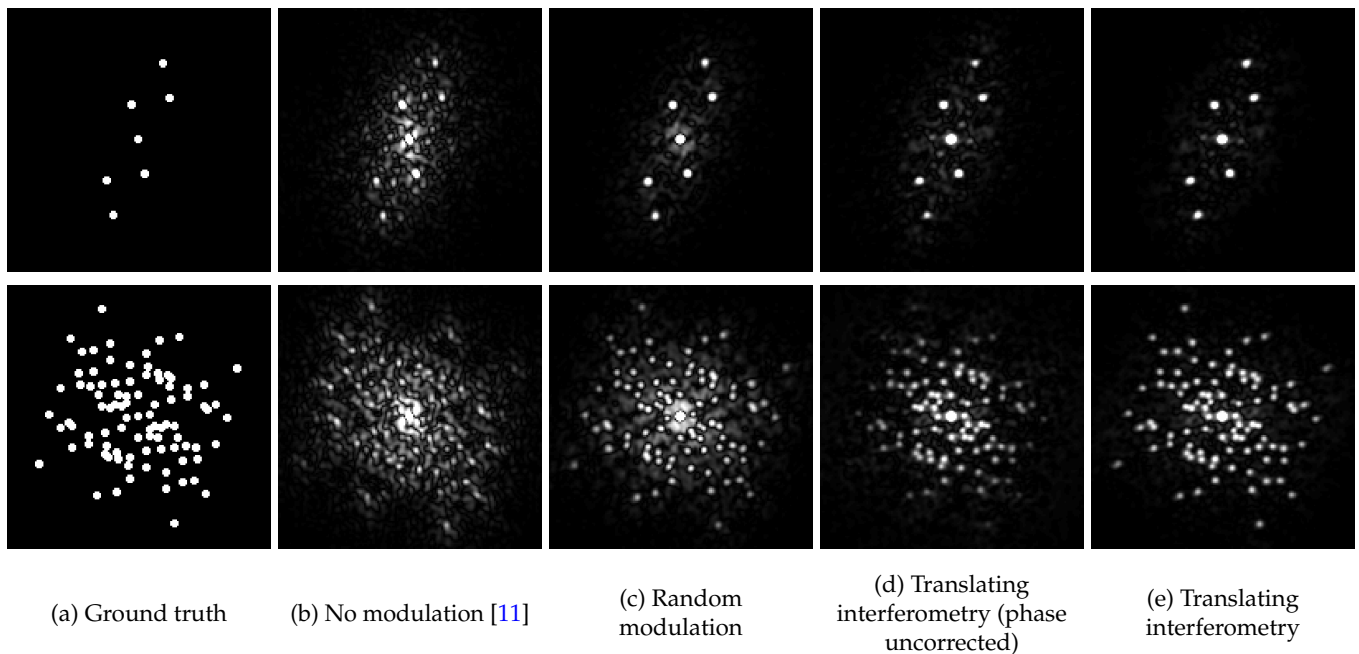


Fig. S6. Comparing speckle auto-correlation in translating interferometry with and without correction. (a) Input. (b) Auto-correlation from a single speckle image with no modulation. (c) Random phase mask in the Fourier plane. (d) Translating interferometry measurements without correction. The larger displacements at the outer image regions are degraded due to phase variations. (e) After phase correction, translating interferometry can recover further displacements.

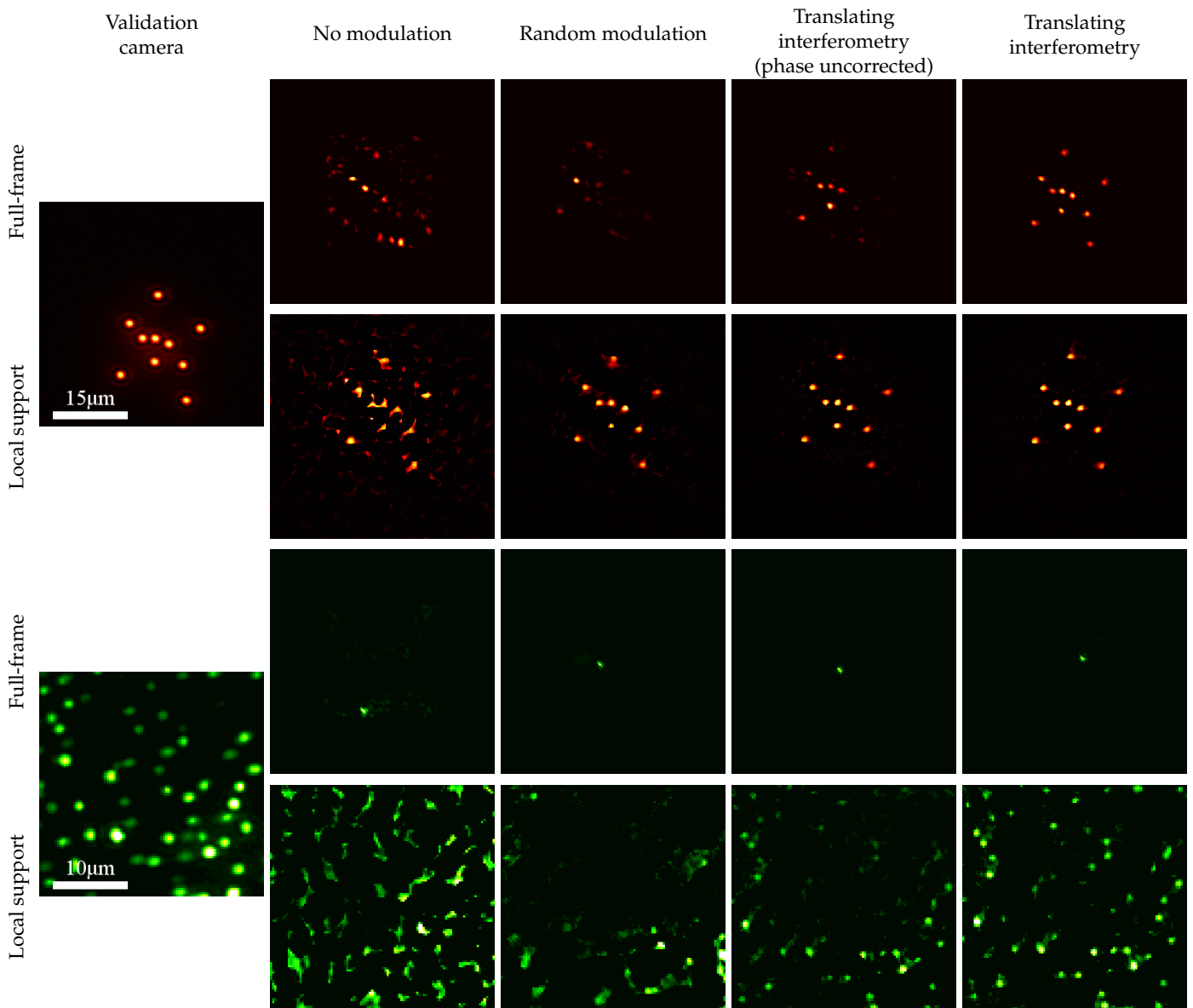


Fig. S7. Comparing translating interferometry with and without phase correction. In addition to Fig. 7, we compare translating interferometry without phase correction. Top part: sparse, simple shifting laser target. Lower part: challenging fluorescent beads target. For the simple target on the top, the full-frame algorithm using the auto-correlation of the translating interferometry measurements without phase correction fails to recover the further beads. The local correlation approach which is more robust to noise can recover the target with and without correlation. For the challenging target at the lower part, the full-frame algorithm fails completely even with phase correction. The local correlations algorithm can reconstruct the target using translating interferometry modulations. However, without phase correction, it can only reconstruct a subset of the beads.

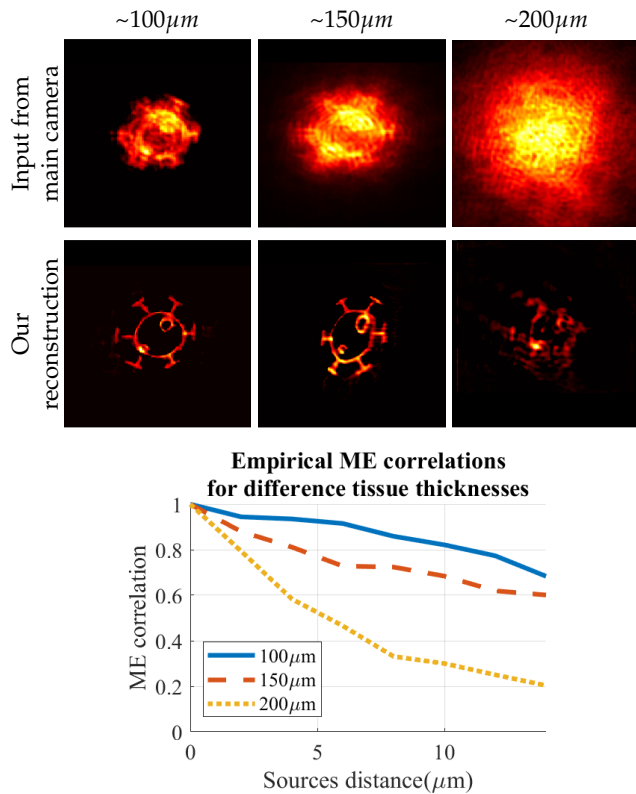


Fig. S8. Compare reconstructions with different tissue thickness. Top panel: We use the shifting laser acquisition to capture the same illumination pattern through three different tissue slices of increasing thicknesses. As tissue thickness increase the spread of the speckles is wider and the statistical correlations are weaker. With the $\sim 200\mu m$ -thick tissue the correlations are too weak and reconstruction fails. Lower panel: As the shifting laser setup allows capturing speckles from individual sources independently, we can empirically compute the decay of speckle correlation as a function of the distance between the sources. Indeed for thicker tissue slices the correlation decays faster as a function of source separation. This explains the reconstruction failure for the $\sim 200\mu m$ -thick tissue example.

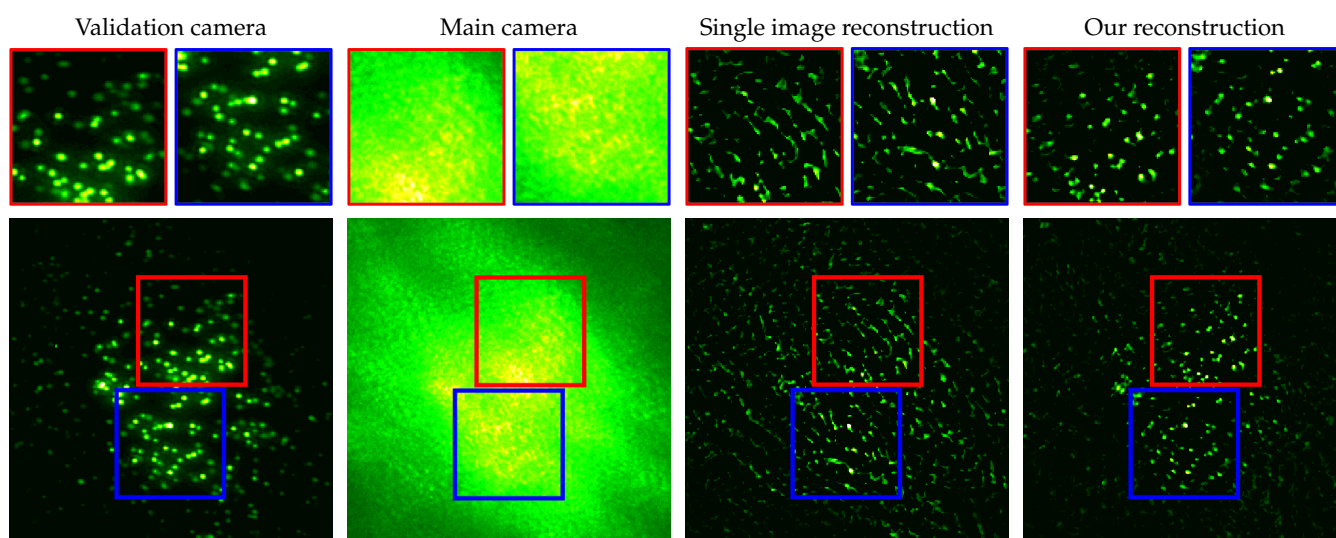


Fig. S9. Additional results. reconstructing fluorescent beads behind a parafilm phantom.